Foam processing and cellular structure of polylactide-based nanocomposites

Yu Ema, Manabu Ikeya, Masami Okamoto *

*Advanced Polymeric Nanostructured Materials Engineering, Graduate School of Engineering, Toyota Technological Institute,
Hisakata 2-12-1, Tempaku, Nagoya 468-8511, Japan*

Abstract

Via a batch process in an autoclave, the foam processing of neat polylactide (PLA) and two different types of PLA-based nanocomposites (PLACNs) has been conducted using supercritical carbon dioxide (CO_2) as a foaming agent. The cellular structures obtained from various ranges of foaming temperature–CO_2 pressure were investigated by using scanning electron microscopy (SEM) and transmission electron microscopy (TEM). The incorporation with nano-clay induced heterogeneous nucleation because of a lower activation energy barrier compared with homogeneous nucleation as revealed by the characterization of the interfacial tension between bubble and matrix. The grown cells having diameter of ~ 200 nm were localized along the dispersed nano-clay particles in the cell wall. The dispersed nano-clay particles acted as nucleating sites for cell formation and the cell growth occurs on the surfaces of the clays. The PLACNs provided excellent nanocomposite foams having high cell density from microcellular to nanocellular.
© 2006 Elsevier Ltd. All rights reserved.

1. Introduction

About 20 years ago, Martini and his colleagues [1] first reported microcellular polymeric foams by using carbon dioxide (CO_2) as a physical-blowing agent. The microcellular foams are closed-cell morphology with a cell density in excess of 10^8 cell/cm^3 and cell diameter in the order of 10 μm. The rationale is that if the cell size is smaller than the critical flaws, which already exist in the bulk polymer matrix could be introduced in sufficient numbers, then the material density could be reduced while maintaining the essential mechanical properties.

Development of nanocomposite foams is one of the latest evolutionary technologies of the polymeric foam through a pioneering effort by Okamoto and his colleagues [2,3]. They prepared poly(L-lactide) (PLA)/clay nanocomposite (PLACN) foams in a batch process by using supercritical CO_2 as a physical foaming agent [4]. However, there are still some controversial data regarding the nucleating effect of the dispersed clay particles.

To innovate on the materials properties of nanocomposite foams, we have to understand the morphological correlation between the dispersed silicate particles with nanometer dimensions in the bulk and the formed closed-cellular structure after foaming. To the best of our knowledge, however, this issue is not very well explored in literatures. There have been no reports for systematic studies on the preparation of nanocomposite foams from microcellular to nanocellular so far.

This paper is devoted to the study on evaluation the performance potential of the PLACNs in foam application. We investigate the cellular foam structure by using scanning electron microscopy (SEM) and transmission electron microscopy (TEM) for neat PLA as a reference material and PLACNs having different types of the dispersion of the nano-fillers.

2. Experimental

2.1. Nanocomposite preparation and characterization

A commercial poly(L-lactide) (PLA) with a D content of 1.1–1.7% ($M_w = 1.87 \times 10^5$, $M_w/M_n = 1.76$, $T_g \sim 60$ °C and $T_m \sim 168$ °C) supplied by Unitika Co. Ltd, Japan was dried under vacuum at 60 °C, and kept under dry nitrogen gas for

---

* Corresponding author. Tel.: +81 52 809 1861; fax: +81 52 809 1864.
E-mail address: okamoto@toyota-ti.ac.jp (M. Okamoto).

1 week prior to use. The molecular weight and thermal properties were determined by gel permeation chromatography and differential scanning calorimeter, respectively, [4].

The organically modified layered silicate (OMLS) having different types of intercalants used in this study were synthesized by replacing Na^+ ions in montmorillonite (MMT) with alkylammonium cations (octadecylammonium (ODA) and octadecyl tri-methylammonium, di-octadecyl di-methylammonium (SBE)) [5]. Nanocomposites (PLACNs) were prepared by melt extrusion. The details of the nanocomposites preparation were described in our previous papers [5]. The dried PLACNs pellets were converted into sheets with a thickness of 0.7–1.5 mm by pressing with ∼1.5 MPa at 190 °C for 3 min using a hot press. The molded sheets were quickly quenched between glass plates and then annealed at 110 °C for 1.5 h to crystallize isothermally before being subjected to various characterizations and foam processing. The nano-structure analyses of wide-angle X-ray diffraction (WAXD) and transmission electron microscopy (TEM) were carried out using the same apparatus as described in the previous articles [4,5].

2.2. Foam processing

The foam processing was conducted on PLACNs and neat PLA in an autoclave (TSC-WC-0096, Taiatsu Techno Co.) by using supercritical CO_2 [4]. Basically, the physical foam processing (batch process) used in this study consists of three stages: (1) CO_2 saturation in the sample at desired temperature; (2) cell nucleation when the release of CO_2 pressure started (supersaturated CO_2) and cell growth to an equilibrium size during the release of CO_2; and (3) cell stabilization via cooling process of the foamed system. In the first stage, the specimen $(5 \times 10 \times 1.5 \text{ mm}^3 = \text{width} \times \text{length} \times \text{thickness})$ was inserted into an autoclave (96 mL) and CO_2 pressure was increased up to 30 MPa at various temperatures. Set-up of the autoclave and temperature–pressure protocol used in this study are shown in Fig. 1. The temperature inside the autoclave was increased and maintained at a predetermined temperature using a band heater for temperature control. In this study, we conducted the experiments at four different foaming temperatures (T_f) (100–150 °C) from just below the melting temperature (T_m) to above the glass temperature (T_g) of matrix PLA. The sample in the autoclave was heated from room temperature to T_f in 0.5 h to achieve the equilibrium state, and then dissolved in CO_2 for 4 h under the pressure range between 14 and 30 MPa. For such a long time of CO_2 dissolution into the sample, CO_2 has already been completely saturated in the sample at fixed T_f. In the second stage, the CO_2 pressure was rapidly reduced in order to supersaturate the specimen with CO_2 gas [4]. The thermodynamic instability resulted in the formation of a large number of cell nuclei. After releasing the CO_2 pressure, the formed foams were stabilized via cooling by liquid-CO_2 to room temperature, and then removed carefully from the autoclave and kept at ambient temperature.
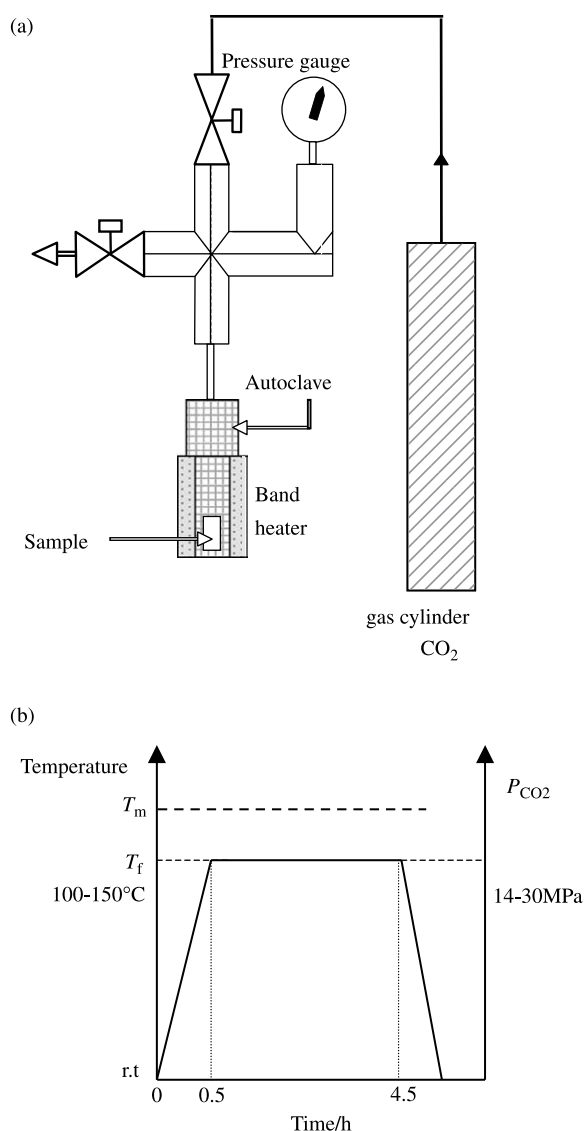

Fig. 1. (a) Schematic representation of autoclave set-up. (b) Temperature and CO_2 pressure protocol used in this study.

2.3. Foam characterization

The cell structures were investigated by using scanning electron microscope (SEM) (JSM-5310LV, JEOL). The samples were freeze-fractured in liquid nitrogen and sputter-coated with gold at an argon pressure of 0.1 Torr for 3 min at a current of 10 mA. We also conducted the morphological analysis by using transmission electron microscopy (TEM) (H-7100, Hitachi Co.), operated at an accelerating voltage of 100 kV. The ultra thin sections (the edge of the sample sheet perpendicular to the compression mold) with a thickness of ∼100 nm were microtomed at −80 °C using a Reichert Ultra cut cryo-ultramicrotome, after suitably staining the sample with 12 tungstophosphoric acid at 80 °C for 5 h. The mass density of both pre-foamed (ρ_p) (=1.258 g/cm³) and post-foamed (ρ_f) in g/cm³ samples were estimated by using the buoyancy method. The average cell radius (d) in mm was determined from the data of SEM observation. All samples
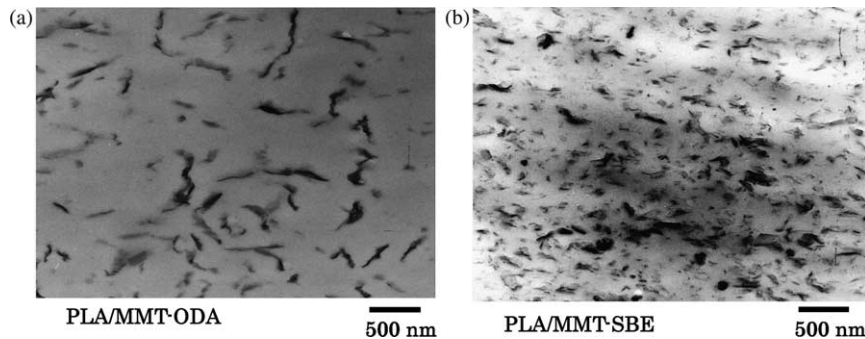
Fig. 2. Bright filed TEM images of PLA-based nanocomposites prepared with (a) MMT–ODA and (b) MMT–SBE. The dark entities are the cross-section and or face of intercalated-and-stacked silicate layers and the bright areas are the matrix.

almost obeyed the Gaussian distribution. The function for determining cell density (N_c) in cell/cm^3 is defined as the following Eq. (1) [2]

$$N_c = 10^4 \frac{3[1 - (\rho_f/\rho_p)]}{4\pi d^3} \qquad (1)$$

On the other hand, the mean cell wall thickness (δ) in μm was estimated by the following Eq. (2) [2].

$$\delta = d(1/\sqrt{1 - (\rho_f/\rho_p)} - 1) \qquad (2)$$

3. Results and discussion

3.1. Nanocomposite structure

Fig. 2 shows the results of TEM bright field images of PLA-based nanocomposites, in which dark entities are the cross-section of intercalated MMT layers. The organically modified MMT content in all nanocomposites was 4 wt%. From the TEM images it becomes clear that there are some intercalated-and-stacked silicate layers in the nanocomposites.

We estimate the form factors obtained from TEM images, the average value of the length (L) of the dispersed particles and the correlation length (ξ) between them [5]. From the WAXD patterns, the crystallite size (D) of intercalated-and-stacked silicate layers of each nanocomposite is calculated by using the Scherrer equation [6]. The calculated value of D ($\cong$ thickness of the dispersed particles) and other parameters for each nanocomposite are presented in Table 1.

For PLA/MMT–SBE, L and D are in the range of 200 and 10.7 nm, respectively. On the other hand, PLA/MMT–ODA exhibits a large value of L (450 ± 200 nm) with a large level of stacking of the silicate layers ($D \sim 21$ nm). ξ value of the PLA/MMT–SBE (80 ± 20 nm) is lower than the value of PLA/MMT–ODA (260 ± 140 nm), suggesting that the intercalated layers are more homogeneously and finely dispersed in case of PLA/MMT–SBE. The number of the stacked individual silicate layers ($\equiv D/d_{(001)} + 1$) is 5 for PLA/MMT–SBE and ξ value of this nanocomposite is one order of magnitude lower compared to those of PLA/MMT–ODA, suggesting that intercalated silicate layers are more homogeneously and finely dispersed. This morphological difference comes from the

degree of the penetration of the PLA chains into the silicate galleries, as discussed in our previous paper [7].

Combining the results of WAXD analyses and TEM observations, we can estimate another parameter L/D, the two-dimensional aspect ratio of the dispersed clay particles. PLA/MMT–ODA exhibits higher enhancement of the ratio of dynamic modulus $G'(G'_{PLACN}/G'_{PLA})$, with large aspect ratio L/D compared to that of PLA/MMT–SBE.

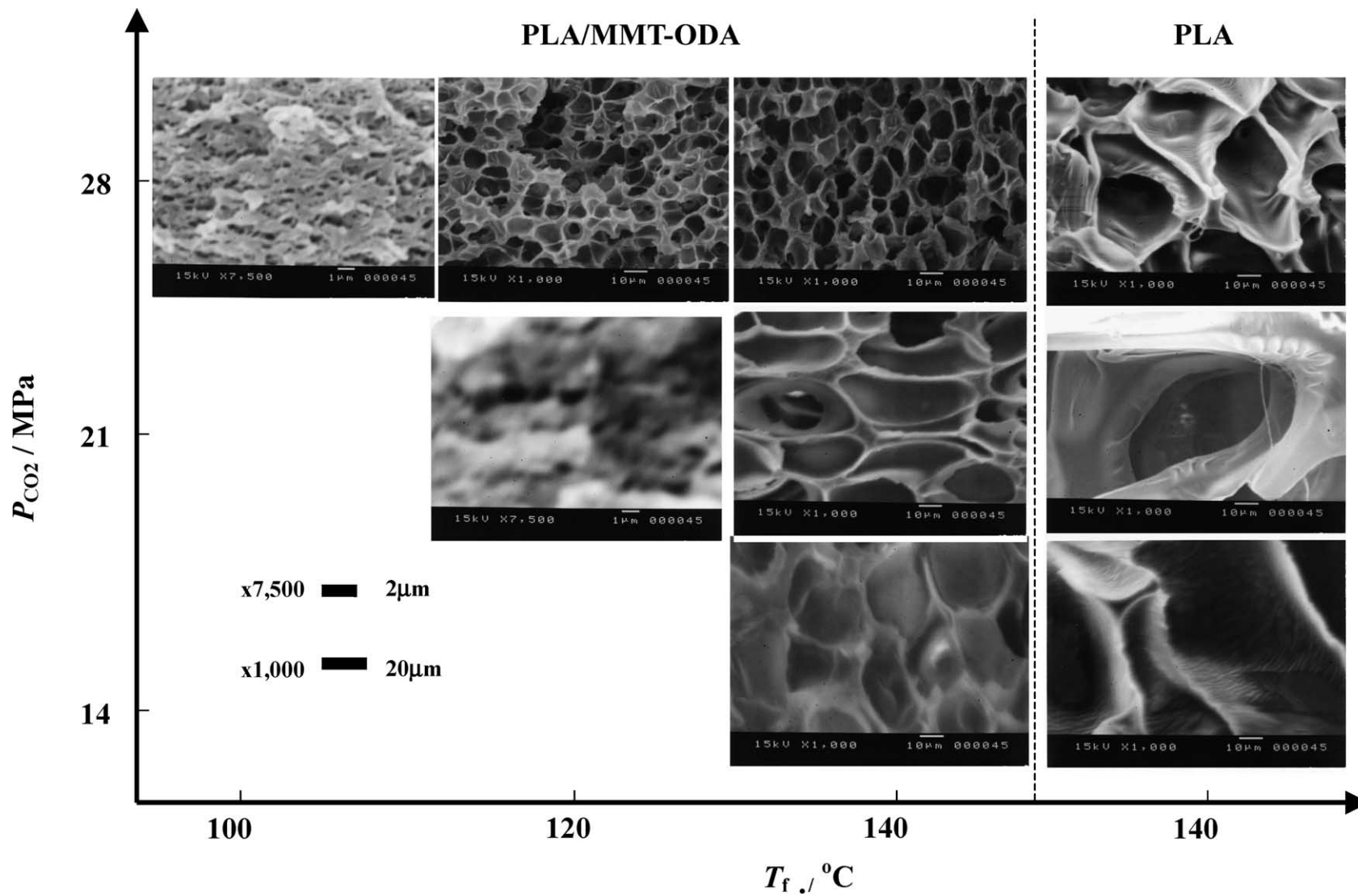### 3.2. Morphology of PLACN foams

Fig. 3 shows the typical results of SEM images of the fracture surfaces of the PLA/MMT–ODA and neat PLA without clay foamed at a temperature range of 100–140 °C under the different isobaric saturation conditions (14, 21 and 28 MPa). All foams exhibit nicely the closed-cell structure. We noted here that homogeneous cells were formed in case of nanocomposite foams, while neat PLA foams show rather non-uniform cell structure having large cell size. The nanocomposite foams show smaller cell size (d) and larger cell density (N_c) compared with neat PLA foam, suggesting that the dispersed silicate particles act as nucleating sites for cell formation [2]. For both foam systems, we have calculated the distribution function of cell size from SEM images and the results are presented in Fig. 4. The nanocomposite foams nicely obeyed the Gaussian distribution. In case of PLA/ODA foamed at 150 °C under high pressure of 24 MPa, we can see that the width of the distribution peaks, which indicates the dispersity for cell size, became narrow accompanied by finer dispersion of silicate particles.

Table 1
Form factors of three nanocomposites obtained from WAXD and TEM observations

Nanocomposites	PLA/MMT–ODA	PLA/MMT–SBE
d_{001} (nm)	3.03	2.85
D (nm)	20.9	10.73
$(D/d_{001}) + 1$	7.9	4.8
L (nm)	450 ± 200	200 ± 25
ξ (nm)	260 ± 140	80 ± 20
L/D	22 ± 9	18 ± 3
G'_{PLACN}/G'_{PLA} [a]	1.65	1.43

[a] G'_{PLACN} and G'_{PLA} are the storage modulus of PLACN and PLA, respectively, at 25 °C.

PLA/MMT-ODA

PLA

P_{CO2} / MPa

28

21

14

x7,500 ▬ 2μm

x1,000 ▬ 20μm

100   120   140   140

T_f ./ °C

15kV X7,500   1μm 000045
15kV X1,000   10μm 000045
15kV X1,000   10μm 000045
15kV X1,000   10μm 000045
15kV X7,500   1μm 000045
15kV X1,000   10μm 000045
15kV X1,000   10μm 000045
15kV X1,000   10μm 000045
15kV X1,000   10μm 000045

Fig. 3. Typical results of SEM images of the fracture surfaces of PLA/MMT–ODA and neat PLA foamed at temperature range of 100–140 °C under different isobaric saturation condition (14, 21 and 28 MPa).
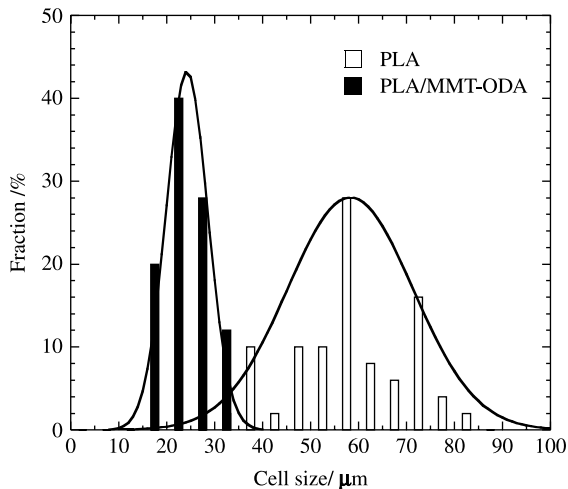
Fig. 4. Typical example for cell size distribution of foamed PLA/MMT–ODA and neat PLA in experiment at 150 °C under 24 MPa. Average values d in μm and variances σ_d^2 in μm^2 in the Gaussian fit through the data are 24.2 and 19.1 for PLA/MMT–ODA foam and 58.3 and 171.0 for PLA foam.

From the SEM images, we have quantitatively calculated various morphological parameters of two different foam systems. At high foaming temperature ($T_f \sim 140$ °C), both PLA/ODA foam and neat PLA foam exhibit the polygon closed-cell structures having pentagonal and hexagonal faces, which express the most energetically stable state of polygon cells. Such foam structure was obtained probably because these foams belong to the polymeric foams having high gas phase volume (>0.7) [3].

Obviously, with decreasing saturation pressure condition (~ 140 °C and 14 MPa), both foams exhibit large cell size due to the low supply of CO_2 molecules, which can subsequently form a small population of cell nuclei upon depressurization. The incorporation of nano-clay (OMLS) induces heterogeneous nucleation because of a lower activation energy barrier compared with homogeneous nucleation [8]. However, the competition between homogeneous and heterogeneous nucleation is no longer discernible. This phenomenon will be discussed later.

3.3. Foaming temperature dependence of cellular structure

The dependence of the foam density (ρ_f) at the T_f under different CO_2 pressure are shown in Fig. 5. Throughout the whole CO_2 pressure range, the mass density of PLA/MMT–ODA foams remains constant value at low T_f range and abruptly decreases beyond a certain T_f, and then attains a minimum constant value up to 150 °C again. From the above results, it can be said that such behavior of mass density is due to the competition between the cell nucleation and the cell growth. At the low T_f range (~ 110 °C), in which a large supply of CO_2 molecules are provided, the cell nucleation is dominant, while at the high T_f, (~ 140 °C), the cell growth and the coalescence of cell are prominent due to low viscosity of the systems compared with the low T_f range (~ 110 °C). This behavior clearly appears in the plots of the cell size ($\cong 2d$), the
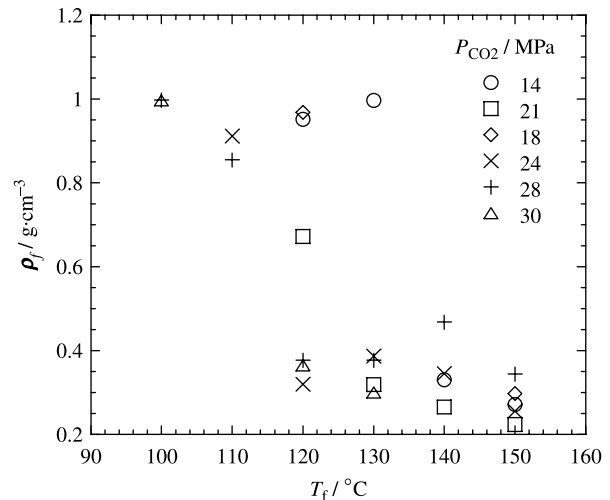

Fig. 5. Foaming temperature dependence of mass density for PLA/MMT–ODA foamed under different CO_2 pressure condition.

cell density (N_c), and the mean cell wall thickness (δ) versus T_f under various pressure conditions, respectively. As seen in Fig. 6, we find that with increasing T_f all nanocomposite foams show an increasing tendency of $2d$ and/or δ and attain a maximum. On the other hand, the temperature dependence of N_c shows opposite behavior compared with the tendency of $2d$
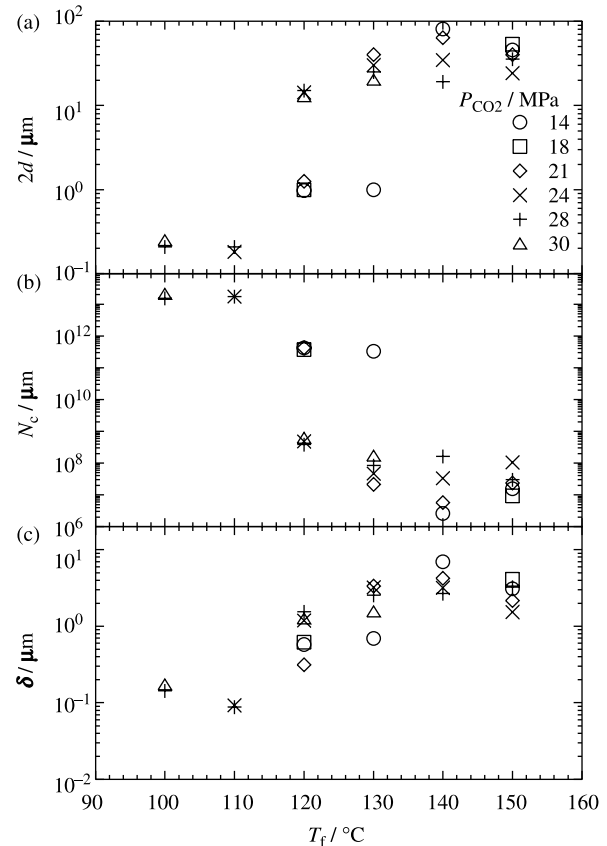

Fig. 6. Foaming temperature dependence of (a) cell size, (b) cell density and (c) mean cell wall thickness under different CO_2 pressure condition.

due to the cell growth and coalescence. Both $2d$ and N_c affect the mass density of the foams.

Using T_g depressions (corresponding to ΔT_g, see Appendix A), we reconstructed plots of ρ_f versus $T_f + \Delta T_g$ from the data of Fig. 5. The results are shown in Fig. 7. We see that all the data, including neat PLA and PLA/MMT–SBE, nicely conform to a reduced curve with $\rho_f \sim 1.0 \pm 0.1$ g/cm³ at $T_f + \Delta T_g <$ 140 ± 4 °C (nanocellular region), whereas ρ_f values approach around 0.3 ± 0.15 g/cm³ as reduced temperature $(T_f + \Delta T_g)$ increased well above 150 °C (microcellular region). The critical temperature is thus 140 ± 4 °C, above which the cell growth prevails. Below the critical temperature, the cell nucleation dominates and the cell growth are suppressed due to the high modulus and viscosity as revealed by the temperature dependence of storage, $G'(\omega)$ and loss, $G''(\omega)$ moduli $(G' = 162$ MPa and viscosity component; $G''/\omega \cong 2$ MPa at 140 °C).

Fig. 8 shows temperature-reduced plots of $2d$, N_c and δ versus $T_f + \Delta T_g$. The all data nicely conform to a reduced curve like Fig. 7. Interestingly, when we use both T_g and T_m [9] depressions to conduct superposition, we have recognized that the reduced curve is nicely constructed but there is no significant difference compare with the case of $T_f + \Delta T_g$. This indicates that T_g depression is important in optimizing foam processing condition but T_m depression may be not a significant factor for processing because the T_f range is still below T_m after CO_2 saturation.

In Fig. 9, we show the relations between $2d$ and N_c, and δ and $2d$ in this study. The relation nicely obeys in Eqs. (1) and (2) but the deviation occurs beyond the value of $N_c \sim 10^{12}$ cell/cm^{-3} for panel (a) and below $2d \sim 1$ μm for panel (b). The downward and upward deviations indicate that the heterogeneous cell distribution mechanism due to the rigid crystalline phases in the PLA matrix is caused by high degree of the crystallinity (~ 49 wt%) under the low foaming temperature range (~ 100 °C). As seen in Fig. 10, the PLACN foams exhibit the heterogeneous cell distribution. The PLA foam reduces the

Fig. 8. Temperature-reduced plots of (a) $2d$, (b) N_c and (c) δ versus $T_f + \Delta T_g$ for PLA/MMT–ODA, PLA/MMT–SBE and neat PLA.

value of N_c accompanied by the large value of δ compared with that of PLACN foams. In case of PLACN foams, the controlled structure of the PLACN foams is from microcellular $(2d \cong 30$ μm and $N_c \cong 3.0 \times 10^7$ cell/cm) to nanocellular $(2d \cong 200$ nm and $N_c \cong 2.0 \times 10^{13}$ cell/cm).

3.4. CO_2 pressure dependence

At high pressure, both homogeneous and heterogeneous nucleation mechanisms may appear to be of comparable significance. All systems demonstrate that N_c increases systematically with increasing CO_2 pressure in the low T_f region (~ 100–120 °C). For PLA/MMT–ODA foams, the system suggests that the heterogeneous nucleation is favor at high pressure condition. The cell nucleation in the heterogeneous nucleation system such as PLA/MMT–ODA foams took place in the boundary between the matrix and the dispersed nano-clay particles. Accordingly, the cell size decreases without individual cell coalescence for PLA/MMT–ODA and neat PLA systems as seen in Fig. 10. To clearly investigate whether the addition of internal surfaces of the dispersed nano-clay may hinder CO_2 diffusion by creating a more tortuous diffusive pathway [5], we conducted the characterization of the interfacial tension between bubble and matrix by using the modified classical nucleation theory [8].

According to the theory proposed by Suh and Colton, the rate of nucleation of cells per unit volume $(\dot{N})$ can
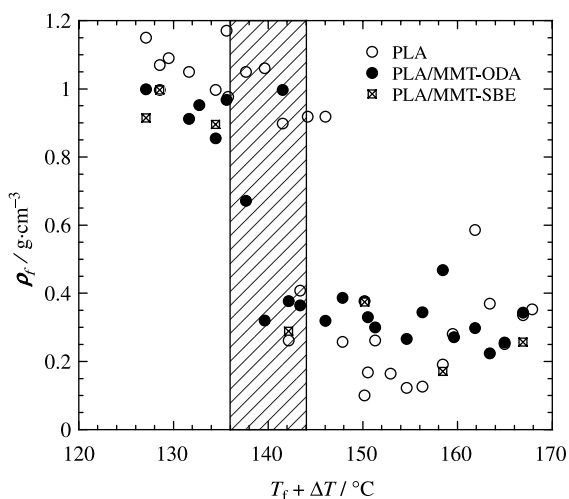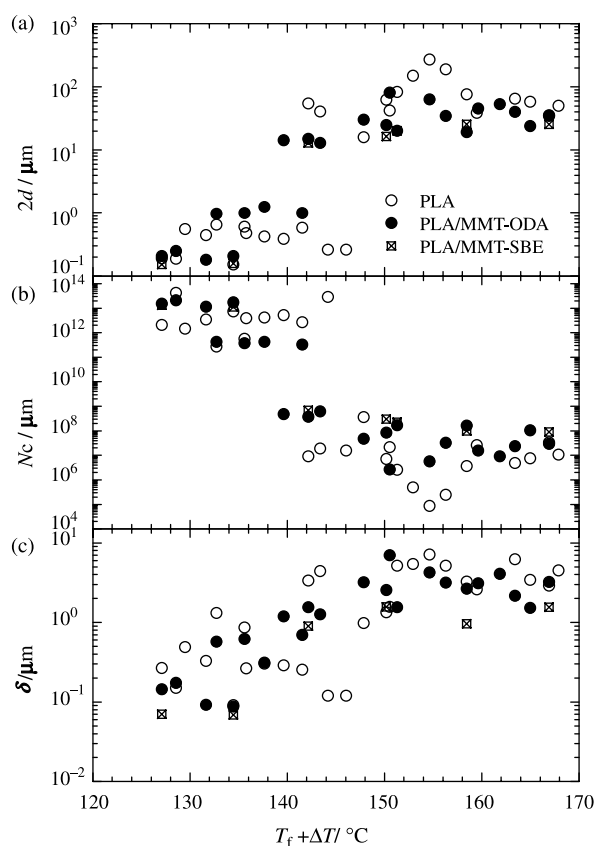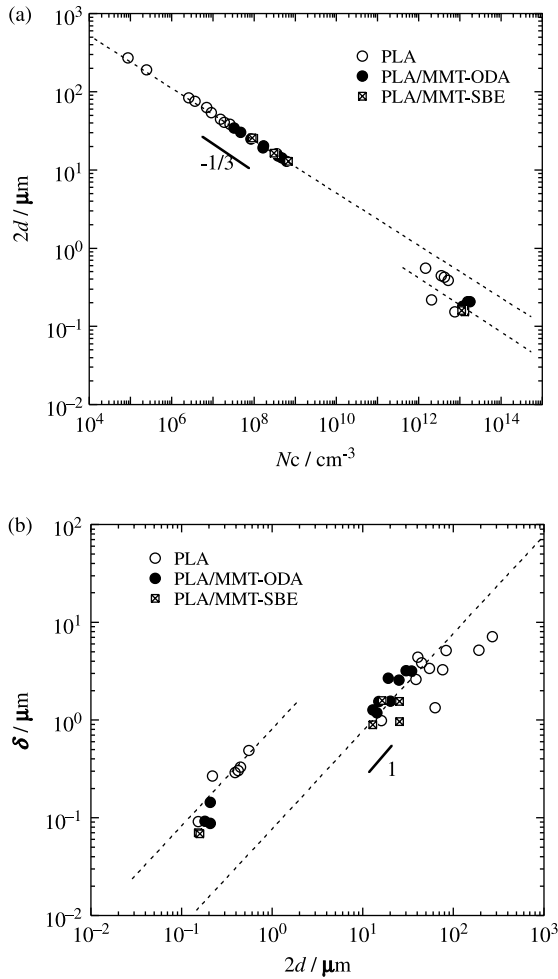

Fig. 7. Plot of mass density for PLA/MMT–ODA, PLA/MMT–SBE and neat PLA versus reduced foaming temperature $(T_f + \Delta T_g)$. The critical temperature $(140 \pm 4$ °C) is shaded.

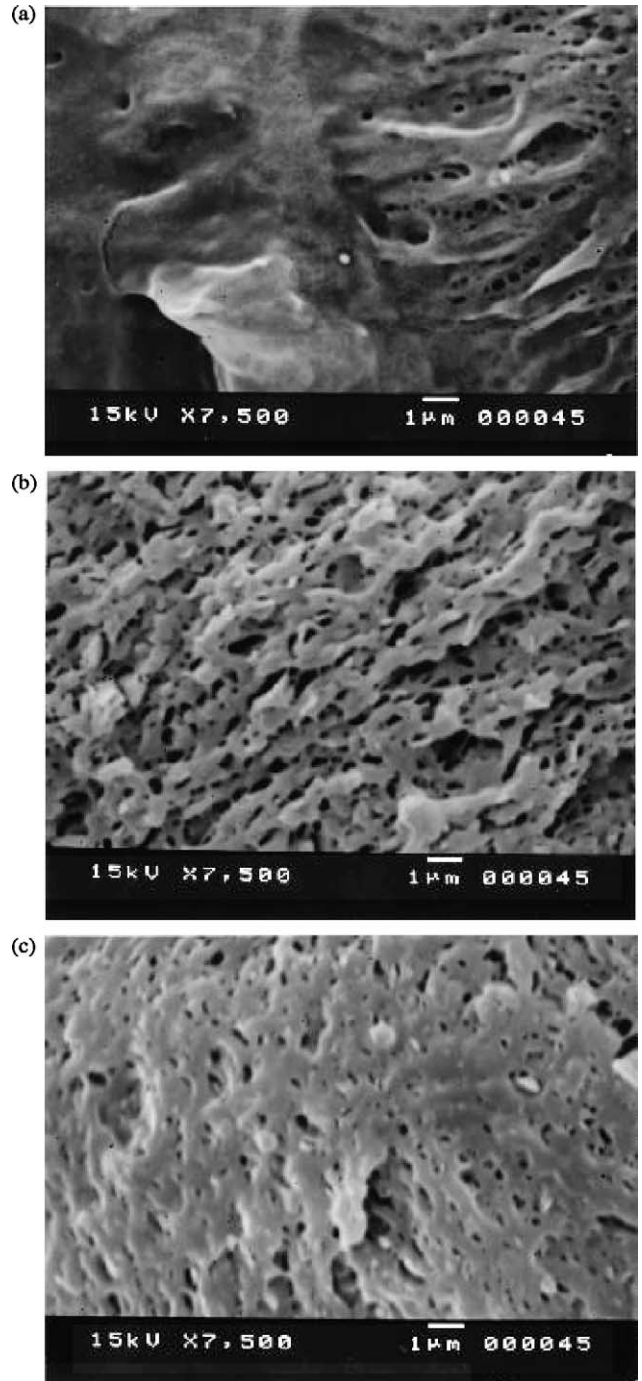Fig. 9. Relation between (a) cell size versus cell density and (b) cell wall thickness versus cell size for all foams.

Fig. 10. SEM images of the fracture surfaces of (a) neat PLA, (b) Pla/MMT–ODA and (c) Pla/MMT–SBE foamed at 100 °C under 28 MPa.

be written as

$$\dot{N} \sim Cf \exp\left[\frac{-16\pi\gamma^3 S(\theta)}{3(\Delta P_{CO_2})^2 k_B T}\right] \tag{3}$$

where C is the concentration of CO_2 and/or the concentration of heterogeneous nucleation sites, f is the collision frequency of CO_2, γ is the interfacial tension between bubble and matrix, $S(\theta)$ is the energy reduction factor for the heterogeneous nucleation (i.e. PLA/MMT–ODA), ΔP_{CO_2} is the magnitude of the pressure quench during depressurization, k_B is the Boltzmann constant, and T is absolute temperature.

The theoretical cell density is given by

$$N_{theor} = \int_0^t \dot{N} dt \tag{4}$$

where t is the foaming time that takes approximately 3 s.

At the low T_f range (110 and 120 °C), the value of N_c increases with ΔP_{CO_2} ($\sim$ 14–28 MPa) because the cell growth is prominent. Assuming no effect of the coalescence of cell on

the value of N_c, we estimate the interfacial tension of the systems calculated using Eqs. (3) and (4), i.e. the slope of the plots (N_c, versus $1/\Delta P_{CO_2}$).

The characteristic parameters of two systems are also summarized in Table 2. The interfacial tension of PLA/MMT–ODA and neat PLA are 6.65 and 7.43 mJ/m² at 110 °C, respectively. These estimated γ values are in good agreement with that of other poly(methyl methacrylate) (PMMA)–CO_2 system ($\sim$ 10 mJ/m²) [10]. We can see that PLA/MMT–ODA

Table 2
Characteristic interfacial parameters of two systems

	T_f (°C)	$\gamma S(\theta)^{1/3}$ (mJ/m^2)	$S(\theta)$	θ (°)
PLA/CO$_2$	110	7.43	1	
PLA/MMT–ODA/CO$_2$		6.65	0.717	107.3
PLA/CO$_2$	120	7.08	1	
PLA/MMT–ODA/CO$_2$		5.38	0.439	85.3

system has a low value compared to that of neat PLA. This trend reflects the relative importance of heterogeneous nucleation, which dominates over homogeneous one in the event that the amount of CO$_2$ available for bubble nucleation is limited because of a lower activation energy barrier, as mentioned before. That is, in the heterogeneous nucleation (PLA/MMT–ODA), we have to take the reduction of the critical energy into consideration because of the inclusion of nucleants, which is a function of the PLA–gas–nano-clay contact angle (θ) and the relative curvature (W) of the nucleant surface to the critical radius of the nucleated phase [11]. In case of $W \geq 10$, the energy reduction factor $S(\theta)$ can be expressed by (Appendix B).

$$S(\theta) = (1/4)(2 + \cos\theta)(1 - \cos\theta)^2 \tag{5}$$

In case of homogeneous nucleation $S(\theta)$ is unity ($\theta = 180°$). The obtained values of the contact angle are 107.3° at 110 °C and 85.3° at 120 °C.

The estimated reduction factor ($S(\theta) = 0.4–0.7$) is not so small when we compared with the other nano-filler (e.g. carbon nanofillers, $S(\theta) = 0.006$) [12]. However, experimentally, nano-clay particles lead to an increase in N_c.

For PLA/MMT–SBE foams prepared under the condition with low T_f ($\sim 100–110$ °C) and high pressure (~ 28 MPa), the nanocomposite foams exhibit no significant difference in N_c compared with PLA/MMT–ODA foams. This reasoning is consistent with the large value of W in both systems.

3.5. TEM observation

To confirm the heterogeneous nucleation and the feature of the nanocellular in the foam processing, we conducted the TEM observation of the cell wall in the PLA/MMT–ODA
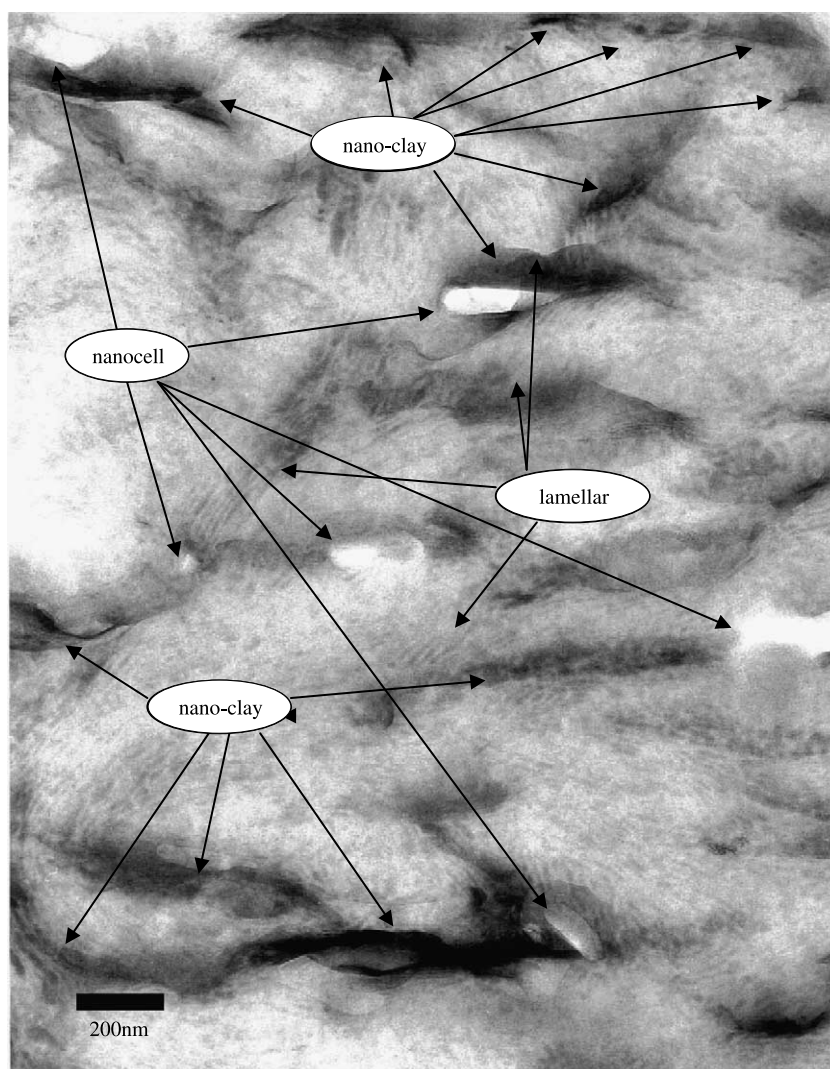

Fig. 11. TEM micrograph for the structure of PLA/MMT–ODA cell wall foamed at 100 °C under 28 MPa.

foam. Fig. 11 shows TEM micrograph for the structure of the cell wall foamed at 100 °C under 28 MPa. Interestingly, the grown cells having a diameter of $\sim$200 nm are localized along the dispersed nano-clay particles in the cell wall. In other words, the dispersed nano-clay particles act as nucleating sites for cell formation and the cell growth occurs on the surfaces of the clays, i.e. the cellular structure is oval-faced morphology rather than spherical cellular structures under high T_f condition ($\sim$140 °C). In Fig. 11, in addition to the nanocellular structure formation, we can observe a lamellar pattern beside the nano-clay particles. This behavior appears to arise from the formation of the α-phase of the PLA crystal in the presence of nano-clay particles [13]. This is a unique observation of the epitaxial crystallization of PLA grown up from clay surfaces due to the nucleation effect of the dispersed nano-clays.

4. Conclusions

Intercalated polylactide (PLA)/clay nanocomposites (PLACNs) have been prepared through the melt intercalation method. The internal structure and morphology of the nanocomposites has been established by using wide-angle X-ray (WAXD) and transmission electron microscopy (TEM), respectively. We have discussed foam processing of intercalated PLACNs by using supercritical CO_2 as a physical foaming agent in a batch process at various temperature and CO_2 pressure ranges. At low foaming temperature ($T_f \sim$ 100–110 °C), the PLA/MMT–ODA foam showed smaller cell size ($2d$), i.e. larger cell density (N_c) compared with neat PLA foams, suggesting that the dispersed clay particles act as nucleating sites for cell formation and lowering of cell size with clay. The incorporation of nano-clay induced heterogeneous nucleation because of a lower activation energy barrier compared with homogeneous nucleation as revealed by the characterization of the interfacial tension between bubble and matrix. Accordingly, PLACN systems provided excellent nanocomposite foam having high cell density at low temperature with high CO_2 pressure condition. The controlled structure of the PLACN foams was from microcellular ($2d \cong 30$ μm and $N_c \cong 3.0 \times 10^7$ cell/cm) to nanocellular ($2d \cong 200$ nm and $N_c \cong 2.0 \times 10^{13}$ cell/cm).

Appendix A

A.1. Dependence of the dissolved CO_2 concentration on T_g

To clearly investigate T_g depression, we should understand the residue of CO_2 in the samples after depressurization. According to Henry's law [14]

$$C_s = H(T)P_{CO_2} \tag{A1}$$

where C_s is the gas concentration at saturation, $H(T)$ is the Henry's law constant and P_{CO_2} is the CO_2 saturation pressure. The temperature dependence of H can be expressed by an
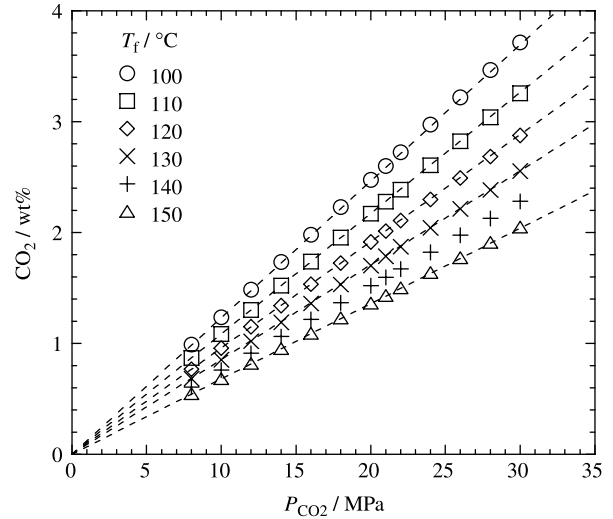

Fig. 12. Equilibrium CO_2 gas concentration versus saturation CO_2 pressure.

Arrhenius-type equation

$$\ln\left(\frac{H(T)}{H_0}\right) = \frac{E_a}{R}\left(\frac{1}{T} - \frac{1}{T_0}\right) \tag{A2}$$

where H_0 is the Henry's constant at 210 °C ($=T_0$) ($=4.90 \times 10^{-3}$ g CO_2/g MPa), which is reported by Takada [9], and E_a is the activation energy ($=15.65$ kJ/mol) [15]. We first determined $H(T)$ in the temperature range of 100–150 °C. Then we determined the gas concentration at various saturation pressures.

Fig. 12 shows some examples of equilibrium gas concentration versus saturation pressure.

Now, we turn our discussion to the T_g depression. According to Chow's model [16], we can predict the T_g of the polymer/gas mixture as follows

$$\ln\left(\frac{T_g}{T_g}\right) = \beta[(1-\vartheta)\ln(1-\vartheta) + \vartheta\ln(\vartheta)] \tag{A3}$$

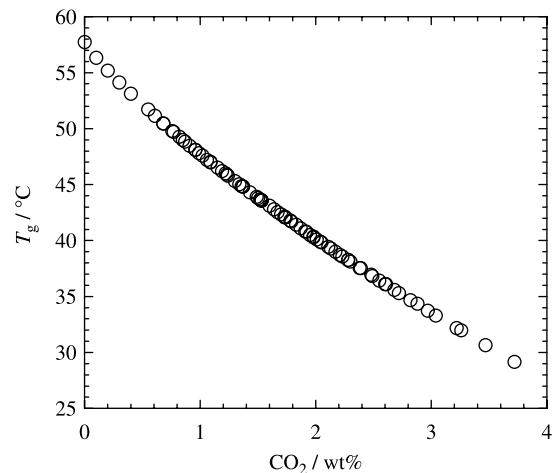$$\vartheta = \frac{M_P}{2M_{CO_2}}\frac{w}{1-w} \tag{A4}$$

Fig. 13. Glass transition temperature depression of matrix PLA versus CO_2 concentration.

where T_{g_0} is the T_g without gas, M_p and M_{CO_2} are the molecular weight of repeating unite in PLA and CO_2, respectively, and w is the weight fraction of gas.

β is related to the heat capacity by

$$\beta = 2R/M_p \Delta C_P \tag{A5}$$

where ΔC_P is the excess transition isobaric specific heat at T_g ($=0.336$ J/gK) [17].

The results are shown in Fig. 13. Increasing the diluent (CO_2) concentration reduces T_g monotonously. High CO_2 pressure condition (30 MPa at 100 °C) provides a large supply of CO_2 molecules (3.72 wt%) where the T_g depression occurs up to 29.2 °C. The significant depression in T_g greatly reduces the melt viscosity and increases the mobility of polymer chains.

As discussed in Figs. 5 and 6, high P_{CO_2} condition ($\sim$30 MPa) corresponds to much higher processing temperature range ($\sim$100+29.2 °C).

Appendix B

The critical size of the nuclei generated at any condition can be calculated by [11]

$$r* = 2\gamma/\Delta P_{CO_2} \tag{A6}$$

where $r*$ is the radius of the critical nuclei. Under the experimental condition, $r*$ is $\sim$0.5 nm.

The relative curvature ($W=L/2r*$) are 450 and 200 with L of 450 nm for PLA/MMT–ODA and L of 200 for PLA/MMT–SBE, respectively, (Table 1). In case of $W \geq 10$, the energy

reduction factor depends on the PLA–gas–nano-clay contact angle. For this reason, we could not observe the filler-size effect on the heterogeneous nucleation, completely diminishing the benefit of nano-clays.

References

[1] Martini, JE. PhD Thesis, Massachusetts Institute of Technology, USA; 1981.
[2] Okamoto M, Nam PH, Maiti M, Kotaka T, Nakayama T, Takada M, et al. Nano Lett 2001;1:503.
[3] Nam PH, Okamoto M, Maiti P, Kotaka T, Nakayama T, Takada M, et al. Polym Eng Sci 2002;42(9):1907.
[4] Fujimoto Y, Sinha SR, Okamoto M, Ogami A, Ueda K. Macromol Rapid Commun 2003;24:457.
[5] Sinha RS, Yamada K, Okamoto M, Ogami A, Ueda K. Chem Mater 2003; 15:1456.
[6] Dritis VA, Tchoubar C. X-ray diffraction by disordered lamellar structures, vol. 99. New York: Springer-Verlag; 1990 p. 21.
[7] Yoshida O, Okamoto M. Macromol Rapid Commun 2006;27:751.
[8] Colton JS, Suh NP. Polym Eng Sci 1987;27:485.
[9] Takada M. PhD Thesis, Crystallization control and foam processing of semi-crystalline polymers via supercritical CO_2, Kyoto University; 2004.
[10] Goel SK, Beckman EJ. Polym Eng Sci 1994;34:1137.
[11] Fletcher NH. J Chem Phys 1958;29:572.
[12] Shen J, Zeng C, Lee LJ. Polymer 2005;46:5218.
[13] Nam JY, Sinha SR, Okamoto M. Macromolecules 2003;36:7126.
[14] Durril PL, Griskey RG. AIChE J 1969;15:106.
[15] Ito Y., Yamashita M., Okamoto M. Macromol Mater Eng; in press.
[16] Chow TS. Macromolecules 1980;13:362.
[17] Mathot VBF. Polymer 1984;25:579.